A New 3D Printed Radial Flow-Cell for Chemiluminescence Detection: Application in Ion Chromatographic Determination of Hydrogen Peroxide in Urine and Coffee Extracts.

Vipul Gupta[a, b], Parvez Mahbub[a], Pavel N. Nesterenko[a], Brett Paull[a, b]*

[a]*Australian Centre for Research on Separation Sciences (ACROSS), School of Physical Sciences, University of Tasmania, Sandy Bay, Hobart 7001, Tasmania, Australia*

[b]*ARC Centre of Excellence for Electromaterials Science, School of Physical Sciences, University of Tasmania, Sandy Bay, Hobart 7001, Tasmania, Australia*

AUTHOR INFORMATION

Corresponding Author

Brett.Paull@utas.edu.au

+61 3 6226 6680

Australian Centre for Research on Separation Sciences (ACROSS), School of Physical Sciences, University of Tasmania, Sandy Bay, Hobart 7001, Tasmania, Australia.

1 ABSTRACT

A new polymer flow-cell for chemiluminescence detection (CLD) has been designed and developed by diverging multiple linear channels from a common centre port in a radial arrangement. The fabrication of radial flow-cell by 3D PolyJet printing and fused deposition modeling (FDM) has been evaluated, and compared with a similarly prepared spiral flow-cell design commonly used in chemiluminescence detectors. The radial flow-cell required only 10 hours of post-PolyJet print processing time as compared to ca. 360 hours long post-PolyJet print processing time required for the spiral flow-cell. Using flow injection analysis, the PolyJet 3D printed radial flow-cell provided an increase in both the signal magnitude and duration, with an average increase in the peak height of 63% and 58%, peak area of 89% and 90%, and peak base width of 41% and 42%, as compared to a coiled-tubing spiral flow-cell and the PolyJet 3D printed spiral flow-cell, respectively. Computational fluid dynamic (CFD) simulations were applied to understand the origin of the higher CLD signal obtained with the radial flow-cell design, indicating higher spatial coverage near the inlet and lower linear velocities in the radial flow-cell. The developed PolyJet 3D printed radial flow-cell was applied in a new ion chromatography chemiluminescence based assay for the detection of H_2O_2 in urine and coffee extracts.

KEYWORDS

Radial flow-cell; 3D printed flow-cell; hydrogen peroxide; Flow injection analysis; chemiluminescence detection; Ion chromatography

ABBREVIATIONS

IC: Ion chromatography

CLD: Chemiluminescence detection

PMT: Photomultiplier tube

CFD: Computational fluid dynamic

IC-CLD: Ion chromatography coupled chemiluminescence detection

FDM: Fused deposition modeling

RANS: Reynolds-averaged Navier–Stokes (RANS)

SST: Shear stress transport

FOX: Ferrous oxidation-xylenol orange

2 INTRODUCTION

Chemiluminescence detection (CLD) is a potential option for the sensitive determination of solutes which do not possess a strong chromophore or fluorophore, which has been used for various applications including clinical, agricultural, to industrial analysis [1-3]. CLD systems have the advantage of requiring relatively simple instrumentation and can offer extremely high sensitivity for certain solutes. A CLD system essentially consists of only two components, (1) a transparent reaction vessel or a flow-cell and (2) a photodetector. The design of CLD flow-cell defines the sensitivity and reproducibility of the detector, as it influences fluid mixing, band dispersion, the amount of emitted light transmitted to the detector, and consequentially the signal magnitude and duration [4]. A flow-cell design which provides these signal enhancements also enables detector miniaturisation by enabling the use of low-cost digital imaging detectors, as compared to expensive high sensitivity photomultiplier tubes.

Usually, CLD flow-cells are produced by simply coiling polymeric or glass tubing in a plane [4-6] or by milling/etching channels into polymeric materials [7-10]. Coiled-tubing based flow-cells have been widely used for CLD in flow injection analysis (FIA) manifolds [11-14]. However, these simple approaches have some disadvantages, including the rigid nature of most suitable tubing, making the formation of the flat spiral cell rather difficult and irreproducible [15]. Greater design flexibility and complexity can be achieved with the use of milling or etching techniques, with these techniques also providing greater fabrication reproducibility, and access to a wider range of materials. However, they have some notable limitations, including limited resolution of closely spaced channels, and inability to

produce complex 3D channel geometries. Such techniques are also not able to produce sealed channels, and thus are rather laborious and time consuming, due to the multiple steps required for the production of the sealed device.

However, these limitations can potentially be overcome with the use of 3D printing techniques, which can provide rapid and simple production of complex CLD flow-cells in a variety of materials. With the continual development of higher resolution 3D printers allowing multi-material printing, these capabilities are expanding rapidly. In terms of the advantages over other fabrication methods, 3D printing offers (1) the ability to print complex three-dimensional architectures, (2) low cost and time efficient production, (3) minimum wastage of material, (4) a "fail fast and often"[16] approach to prototyping, customisation, and testing, and (5) fabrication of monolithically integrated systems. Accordingly, 3D printing is rapidly becoming a method of choice for both research and industrial fabrication of polymeric and metal based macro- and micro-fluidic devices [17-19]. Use of 3D printing in the production of CLD flow-cells has been recently investigated by Spilstead et al. [20]. However, in this preliminary work, due to the tortuous nature of the spiral flow-cell design investigated, the 3D printing process resulted in only partially cleared (of support material) internal channels [20]. This resulted in significant flow-cell staining, which was presumed to be due to the formation of Mn(IV) on the remaining wax support material in the channels. Accordingly, to obtain the support material free channels, they had to print incomplete channels, and later seal them with transparent films[20]. This obviously negated one of the core advantages of 3D printing and illustrated unsuitability of tortuous flow-cell designs in allowing 3D printing fabrication of analytical flow-cells.

Many varied CLD flow-cell designs have been reported to-date, and the following represents some of the key designs investigated/developed: (1) the most commonly used spirally coiled tubing based flow-cell by Rule et al. [6]; (2) the fountain flow-cell design by Scudder et al. [21], where fluid radially flows between two parallel plates without any channels; (3) the sandwich flow-cell by Pavón et al. [22], which is a membrane based flow-cell; (4) liquid core waveguide based luminescence detectors by Dasgupta et al. [23], which utilise fluoropolymer tubing; (5) the bundle flow-cell by Campíns-Falcó et al. [24], which is based on the random packing of a tube; (6) the vortex flow-cell by Ibáñez-García et al. [25], which consists of a micromixer based on a vortex structure; (7) the serpentine flow-cell by Terry et al. [10], which consists of reversing turns, and finally (8) the droplet flow-cell by Wen et al. [26], which is based on the formation of a small droplet in front of the photodetector.

Many of the above mentioned flow-cell designs, including the spiral, serpentine, and bundle flow-cells, exhibit complex and tortuous geometries, which would present similar difficulties in terms of 3D printing based fabrication as those discussed above [20]. Whereas, simpler flow-cell designs, such as the fountain flow-cell has resulted in inferior CLD performance with a lower signal intensity and a poor signal reproducibility [10]. These issues suggest the need for a new CLD flow-cell design, which is less tortuous than the conventional flow-cells, enabling 3D printing, while still providing a reproducibly response, ideally of higher signal magnitude and duration to the above alternative designs. Thus herein, a new flow-cell has been designed, developed, and evaluated in comparison with the most commonly used spiral flow-cell design for CLD. The new flow-cell has been designed by diverging

multiple linear channels from a common centre port in a radial arrangement and hence named as a 'radial' flow-cell. This radial flow-cell has been produced using both 'PolyJet' and fused deposition modeling (FDM) 3D printing techniques. It has been evaluated and compared quantitatively to a similarly proportioned spiral flow-cell design on the basis of (1) simplicity of fabrication with the 3D PolyJet printing and the FDM printing techniques and (2) CLD performance using the cobalt catalysed reaction of H_2O_2 with luminol as the model system. The flow behaviour in the radial flow-cell and spiral flow-cell designs have been simulated through computational fluid dynamic (CFD) calculations to understand the underlying mechanism for the observed differences in the CLD signals obtained. Finally, to investigate the practical application of the developed radial flow-cell, it was evaluated within an ion chromatographic based assay for the analysis of H_2O_2 in urine and coffee extract.

3 MATERIALS AND METHODS

3.1 Materials

Luminol (Sigma-Aldrich, MO, USA), $CoCl_2$ (Univar, IL, USA), Na_3PO_4 $7H_2O$ (Mallinckrodt, Surrey, UK), NaOH (BDH, PA, USA), H_2O_2 (Chem-Supply Pty Ltd, South Australia, Australia), 5-sulphosalicylic acid (Sigma-Aldrich, MO, USA), ferrous ammonium sulphate ($FeSO_4(NH_4)_2SO_4.6H_2O$) (England, UK), H_2SO_4 (Merck, VIC, Australia), xylenol orange (Sigma-Aldrich, MO, USA), Sorbitol (BDH, PA, USA), 0.45 µM PTFE captiva syringe filters (Agilent, CA, USA). Deionised water purified through a Milli-Q water purification system (Millipore, MA, USA) with a final resistance of 18.2 MΩ was used for all preparations unless mentioned otherwise.

3.2 3D printing

The flow-cells and the black boxes were designed with the Solidworks 3D modelling and CAD software 2014-2015 (Dassault Systèmes SE, France). The PolyJet printed flow-cells were fabricated using an Eden 260VS PolyJet 3D printer (Stratasys, VIC, Australia) with VeroClear-RGD810 resin (Stratasys, VIC, Australia) as the build material and SUP707 (Stratasys, VIC, Australia) as the support material. Post-PolyJet printing, the support material was removed by soaking and intermittent sonication of the flow-cells in a 2% w/v NaOH solution. The FDM printed flow-cells and the black boxes were fabricated using a Felix 3.0 Dual Head FDM 3D printer (IJsselstein, Netherlands) using clear ABS and black PLA filament (Matter Hackers, CA, USA), respectively.

3.3 UV-VIS spectroscopy

UV-VIS spectroscopy was performed on the PolyJet printed chips using SP8001 UV-VIS spectrophotometer (Metertech, Taipei, Taiwan). Rectangular chips were designed and printed to fit inside a standard quartz cuvette filled with Millipore water. The UV-VIS spectroscopy was performed from 200 nm to 1000 nm and the transmittance was recorded while using Millipore water as the blank.

3.4 Flow injection analysis based chemiluminescence setup

A FIA setup for the CLD of H_2O_2 was established using an in-house built pneumatic assembly for pumping the sample carrier (water) and the reagent (luminol-Co(II)) streams, a six port injection valve (VICI Valco, TX, USA) with 2 μL injection loop, a MINIPULS 3 peristaltic pump (Gilson, WI, USA) to fill the injection loop with the sample (H_2O_2), a T-piece to mix the reagent with the sample, 1/16" OD and 0.008" ID

PTFE tubing (IDEX Health & Science (Kinesis), Qld, Australia), and short tefzel nut 1/16 black (IDEX Health & Science (Kinesis), Qld, Australia). Each flow-cell and a R960 Photomultiplier tube (PMT) (Hamamatsu (Stantron), NSW, Australia) were enclosed in a light tight dark box. The PMT signal was recorded with respect to time through a Powerchrome 280 system (eDAQ, NSW, Australia) by converting the produced current into voltage through an online resistor. The luminol-Co(II) reagent was prepared as described previously [27].

3.5 Computational fluid dynamic simulations

Computational fluid dynamic simulations were performed using ANSYS 17.0 software with CFX solver. The radial and spiral flow-cell designs were meshed similarly, resulting in the number of nodes as 4 million and 6 million, respectively. Reynolds-averaged Navier–Stokes (RANS) simulations were performed using the shear stress transport (SST) turbulence model with water as the fluid material. A no-slip wall condition with a roughness of 20 µm was prescribed for the walls. The iterations were manually observed for the convergence of the turbulence kinetic energy, velocity, pressure, and shear stress user points. On successful completion of each run, the results were analysed as required with the CFX-Post.

3.6 FOX assay

A ferrous oxidation-xylenol orange (FOX) assay reagent was prepared following the recipe reported by Yuen et al.[28]. Briefly, 1 mL of ferrous ammonium sulphate solution was mixed with 100 mL of xylenol orange-sorbitol solution. The ferrous ammonium sulphate solution was prepared by dissolving 25 mM ferrous ammonium sulphate in 2.5 M H_2SO_4. The xylenol orange-sorbitol solution was prepared by

dissolving 125 µM of xylenol orange and 100 mM of sorbitol in water. The FOX reagent was freshly prepared just before each analysis. The FOX assay itself involved adding 100 µL of a sample to 1 mL of the FOX reagent into 2 mL amber coloured centrifuge vials (Eppendorf, Hamburg, Germany), which were incubated at room temperature for 20 min (Pierce Chemical Company, Rockford, USA). The absorbance of each sample at 560 nM was measured against a reference blank using the above-mentioned UV-VIS spectrophotometer.

3.7 Ion chromatography

The chromatographic analysis was performed using Waters Alliance 2695 HPLC system (Waters, MA, USA), controlled with Empower Pro software using IonPac®, using the following columns: IonPac CG10 (column size: 50 x 4 mm ID, particle size: 8.5 μm), IonPac CG11 (column size: 50 x 2 mm ID, particle size: 7.5 μm), and IonPac CS11 (column size: 250 x 2 mm ID, particle size: 7.5 μm) (Thermo Fisher Scientific, MA, USA). The column temperature was maintained at 24 ℃ and the sample temperature was maintained at 4 ℃. An injection volume of 10 µL was used. Isocratic separation of H_2O_2 was performed using 100% water as the mobile phase at a flow rate of 800 µL min^{-1} and a 5 min post-run clean-up was performed with 100 mM NaCl at a flow rate of 1 mL min^{-1}. UV detection was performed with Waters 996 PDA detector (Waters, MA, USA) at 210 nm. CLD was performed as described above. Both UV and CLD were performed during separate runs to prevent any degradation of H_2O_2 due to UV exposure. A pneumatic pressure of 200 kPa (~800 µL min^{-1}) was used for the luminol-Co(II) reagent stream.

3.8 Urine analysis

On spot midstream urine samples were collected from a non-fasting healthy individual male and were analysed within 30 mins (including pre-sample treatment). Urine samples were collected in an aluminium foil lined 20 mL glass vial, and were centrifuged and protein precipitated in 2 mL amber centrifuge vials. Centrifugation was performed in an Eppendorf 5424 centrifuge (Eppendorf, Hamburg, Germany).

3.9 Coffee analysis

Freshly grounded coffee beans were extracted on a Café Expresso II coffee machine (Sunbeam, NSW, Australia), using 19 g of coffee powder and made to a final volume of 220 mL. Coffee was brewed in drinking water following the same procedure as typically used to make coffee. Coffee samples were analysed immediately, without any further treatment.

4 RESULTS AND DISCUSSION

4.1 Flow-cell designs

The radial flow-cell was developed by arranging 16 channels in a parallel radial arrangement as shown in Figure 1 (a). All channels were designed with a 700 μm ID and were connected to a common inlet at the centre and a common outlet galley of 1800 μm ID at the circumference. The galley exited with a single outlet of 1500 μm ID. The galley and outlet dimensions were optimised empirically with the help of computational fluid dynamic (CFD) simulations and visual inspection, by pumping a food dye, to prevent any re-circulation from the galley into the channels. Each individual channel consisted of (1) a 3.63 mm long linear section and (2) a 1.62 mm

long curved section with a fillet radius of 1.5 mm near the inlet and a total flow-cell volume of 32 µL as shown in Figure 1 (a). The channel lengths were designed to completely occupy the PMT window, and the galley was kept out of the PMT window. A bottom layer of 1 mm thickness was included to provide robustness, allowing the use of flow-cells up to at least a pressure of 2 MPa. Both the inlet and the outlet were connected to a ¼ unified fine pitch thread (UNF) port to enable a unibody design and allow their easy assembly and disassembly within any conventional FIA manifold.

A conventional coiled-tubing flow-cell was fabricated by spirally coiling a 1/16" OD and 0.02" ID PTFE tubing within a circular diameter of 10 mm and a total flow-cell volume of 13 µL. The coiled-tubing based flow-cell was glued to a black platform, which was trimmed to fit in a similar black box as used with the 3D printed flow-cells as described below. Additionally, a spiral flow-cell design with the similar outer diameter and the number of turns as of the coiled-tubing flow-cell was developed for 3D printing, as shown in Figure 1 (b), to allow closer comparison with the radial flow-cell. The 3D printed spiral flow-cell was developed using an Archimedes spiral with an inner diameter of 1 mm, an outer diameter of 10 mm, a pitch of 1.20 mm, and a total flow-cell volume of 25 µL. The channel inner diameter, outer diameter, and the bottom layer thickness of the spiral flow-cell were kept as similar as possible to the radial flow-cell. The spiral was connected to an inlet at the centre and an outlet at the end. Both the inlet and the outlet were again connected to a ¼ UNF threaded port.

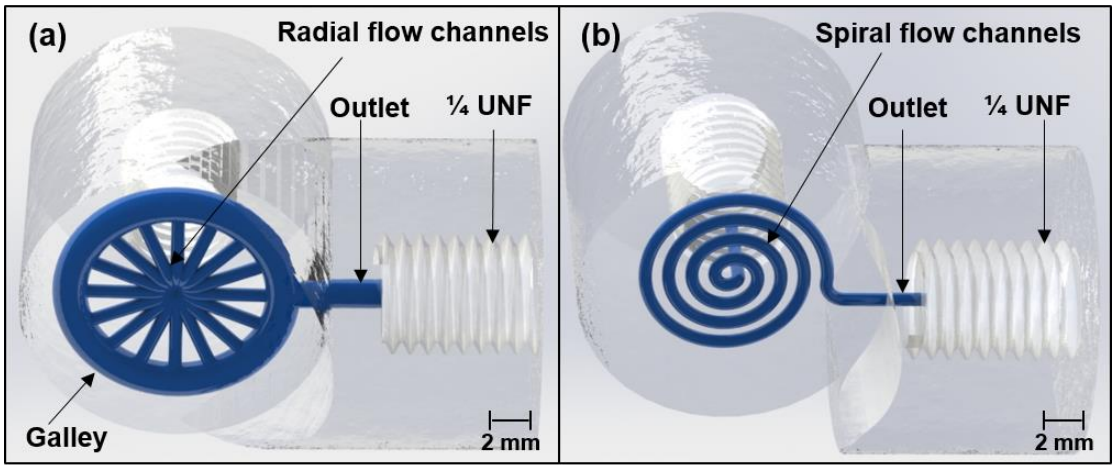

Figure 1. Chemiluminescence flow-cells: (a) render of the 3D printed radial flow-cell and (b) render of the 3D printed spiral flow-cell.

4.2 3D printing

Two complimentary 3D printing techniques, namely PolyJet printing and FDM were applied to the fabrication of radial and spiral flow-cells. The PolyJet printing technique utilises foreign support material and hence allows fabrication of complex structures, whereas, the FDM printing technique can be used without any support material, allowing easy fabrication of simple structures. The use of PolyJet printing for the production of a spiral flow-cell has been previously discussed by Spilstead et al. [20]. They highlighted the issue of incomplete removal of the wax support material from the flow channels as mentioned above. In the current work, this limitation was overcome with the use of a water-soluble support material, namely SUP707. Use of the SUP707 support material as opposed to the wax support material facilitated its complete removal from the tortuous flow channels. However, complete removal of the support material from the 3D printed spiral flow-cell required soaking and intermittent sonication in a 2% (w/v) NaOH solution for ca. 360 hours. This lengthy cleaning protocol enabled the direct formation of closed and completely clear flow-

cell channels. Complete removal of the support material was confirmed by visual inspection, lack of channel staining, and a reproducible signal from successive injections of H_2O_2.

As compared to the spiral design, the radial flow-cell was found to be free of any support material within 10 hours, applying the same post-processing protocol. The significant reduction in time required for removal of the support material from the radial flow-cell was facilitated by the linear configuration of the channels, the presence of wide galley providing additional solvent reserve in the flow-cell, the availability of two entry points for the solvent into each channel that are inlet and galley, and the parallel arrangement of the channels allowing simultaneous cleanup of multiple channels. These features allowed successful 3D fabrication of the radial flow-cell with flow channels of less than 500 µm ID, whereas a spiral flow channel of less than 700 µm ID required more than a month to fully remove the water soluble support material. This greatly reduced post-processing time enabled the entire process of fabrication and post-processing to be accomplished in under a day. Attempting the fabrication of the 700 µm ID spiral flow-cell with an FDM printer resulted in complete channel collapse and blockage, whereas FDM fabrication of the 700 µm ID radial flow-cell resulted in a successful print with open channels.

4.3 PolyJet printed chemiluminescence detection flow-cells

PolyJet printing was the only technique that allowed successful fabrication of both the radial and spiral flow-cells. Accordingly, the PolyJet printed flow-cells were used for the remainder of the study. The optical transmittance of PolyJet printed chips was studied to evaluate the suitability of PolyJet printed flow-cells for the CLD of H_2O_2

using luminol-Co(II) reagent. The chemiluminescence emission wavelengths from the H_2O_2 and luminol-Co(II) reaction range from 380 nm to 600 nm [29]. Accordingly, the transmittance of PolyJet printed chips was recorded for wavelengths ranging from 200 nm to 1000 nm. As shown in Figure 2, 1 mm and 100 µm thick PolyJet printed chips resulted in 89% and 94% transmittance, respectively at 430 nm (highest emission wavelength of H_2O_2-luminol-Co(II) chemiluminescence reaction [29]). The transparency of these flow-cells can be further improved in future through various surface treatments such as polishing, polydimethylsiloxane coating, polystyrene coating, etc. [30]. PolyJet printed flow-cells were transparent in nature and lacked any reflective or opaque backing. Accordingly, black boxes were designed for each flow-cell to (1) provide an opaque backing, (2) ensure a light tight environment around the flow-cell and the PMT, and (3) closely align the flow-cell and the PMT. The black box was designed and 3D printed in two parts (a top and a bottom half) with negative contours to that of the respective flow-cell, as shown in the Supporting information Figure S-1. Holders were included for the PMT and the screws. Both parts were sealed together through a 3D printed lego-type interlock between them. A tight seal was observed between the two halves of the black box and the black box, the flow cell, and the PMT.

The PolyJet resin used in this work was an acrylate based polymer composed of complex mixture of monomers including exo-1,7,7-trimethylbicyclo[2.2.1]hept-2-yl acrylate or acrylic acid isobornyl ester (CAS 5888-33-5, 20-30%); tricyclodecane dimethanol diacrylate (CAS 42594-17-2, 15-30%); 2-hydroxy-3-phenoxypropyl acrylate (CAS 16969-10-1), 4-(1-oxo-2propenyl)morpholine (CAS 5117-12-4); Bisphenol A containing acrylate oligomer treated with epichlorohydrin (5-15%), and

2,4,6-trimethylbenzoyldiphenylphosphine oxide as photoinitiator (0.1-2%) [31]. The polyacrylates should provide reasonable chemical resistance to most dilute acids, bases and oils. However, their use with organic solvents is not recommended as per the known incompatibilities of acrylates with organic solvents. Repetitive injections of 10 μM H_2O_2 at a rate of 150 injections per hour resulted in reproducible chemiluminescence signal with an RSD (n=13) of 1.01% and 0.91% with the use of the 3D printed radial flow-cell and the 3D printed spiral flow-cell, respectively as shown in Figure 3. This indicates the absence of any flow-cell staining or carryover effects, and an ability to perform high throughput CLD studies with the use of these 3D printed flow-cells. In terms of stability, no visible signs of damage were observed to either the 3D printed spiral or 3D printed radial flow-cells throughout this entire study, which was performed over a period of more than one year, with more than 1000 injections on each flow-cell.

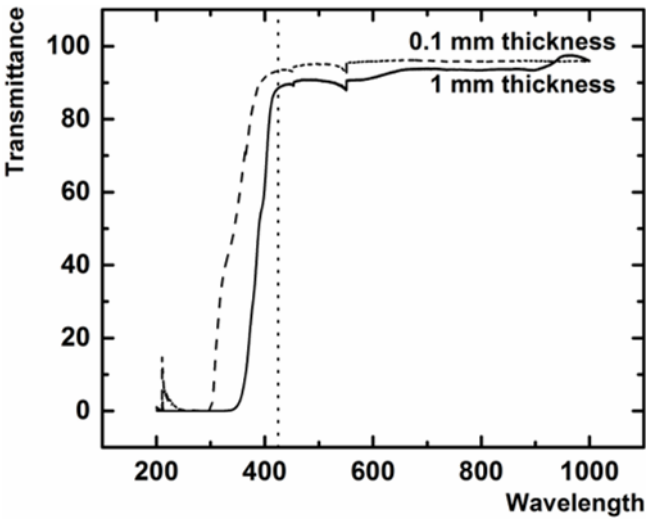

Figure 2. UV-VIS transmittance of the PolyJet 3D printed 1 mm and 0.1 mm thick chips.

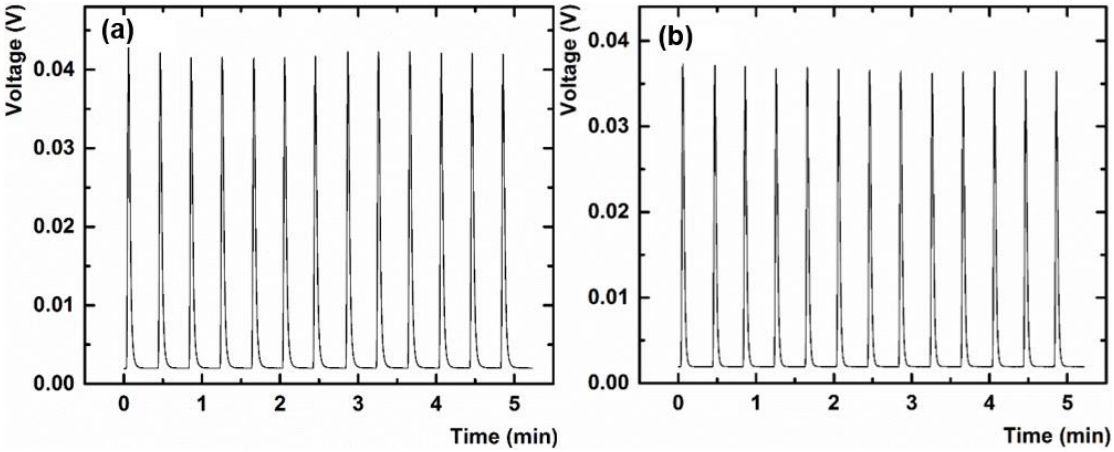

Figure 3. Successive FIA injections of 10 µM H_2O_2 using the PolyJet 3D printed (a) radial flow-cell and (b) spiral flow-cell.

4.4 Chemiluminescence system optimisation

An FIA-chemiluminescence system was setup as shown in Figure 4 (a). Its various parameters were optimised to obtain the maximum reproducible signal intensity. Following our previous work [32], 50 mM Na_3PO_4 at pH 12 was used to prepare the luminol-Co(II) chemiluminescence reagent. Following the previous work of Greenway et al. [33] and Marle et al. [34], 10 µM $CoCl_2$ solution was used to obtain the maximum reproducible signal intensity while avoiding any precipitation. The luminol concentration and the carrier/reagent flow rate ratio were optimised experimentally through iterative univariate analysis since their optimum values were mutually dependent. This provided an optimum luminol concentration of 0.29 mM as shown in Figure 4 (b) and an optimum pneumatic pressure ratio of 1.4 as shown in Figure 4 (c). Accordingly, a luminol-Co(II) solution with 0.29 mM luminol and 10 µM $CoCl_2$ solution in 50 mM Na_3PO_4 buffer with pH 12 was used as the chemiluminescence reagent. As shown in Figure 4 (d), the maximum reproducible signal intensity was observed at the highest total (carrier stream + reagent stream) flow rate. This is presumably due to (1) the higher resultant turbulence at the T-piece,

which facilitates better mixing of the sample and the reagent and (2) rapid transfer of the chemiluminescence products from the T-piece to the flow-cell. Accordingly, a pneumatic pressure of 160 kPa was used for the carrier stream. As per the optimised carrier/reagent pneumatic pressure ratio of 1.4, the reagent stream pneumatic pressure should be 114 kPa. However, the here used pneumatic assembly only allowed to reproducibly obtain pressures in the integer multiples of 10. Hence, pneumatic pressures of 110 kPa, 120 kPa, and 130 kPa were investigated for the reagent stream. No significant difference in the signal intensity was observed between these three reagent stream pneumatic pressures, however, a slightly better reproducibility was observed at 130 kPa. The total volumetric flow rate (carrier + reagent) was observed to be ca. 800 µL min^{-1}. The initial optimisation studies were performed with the 3D printed spiral flow-cell and the final results were verified for all three types of flow-cells.

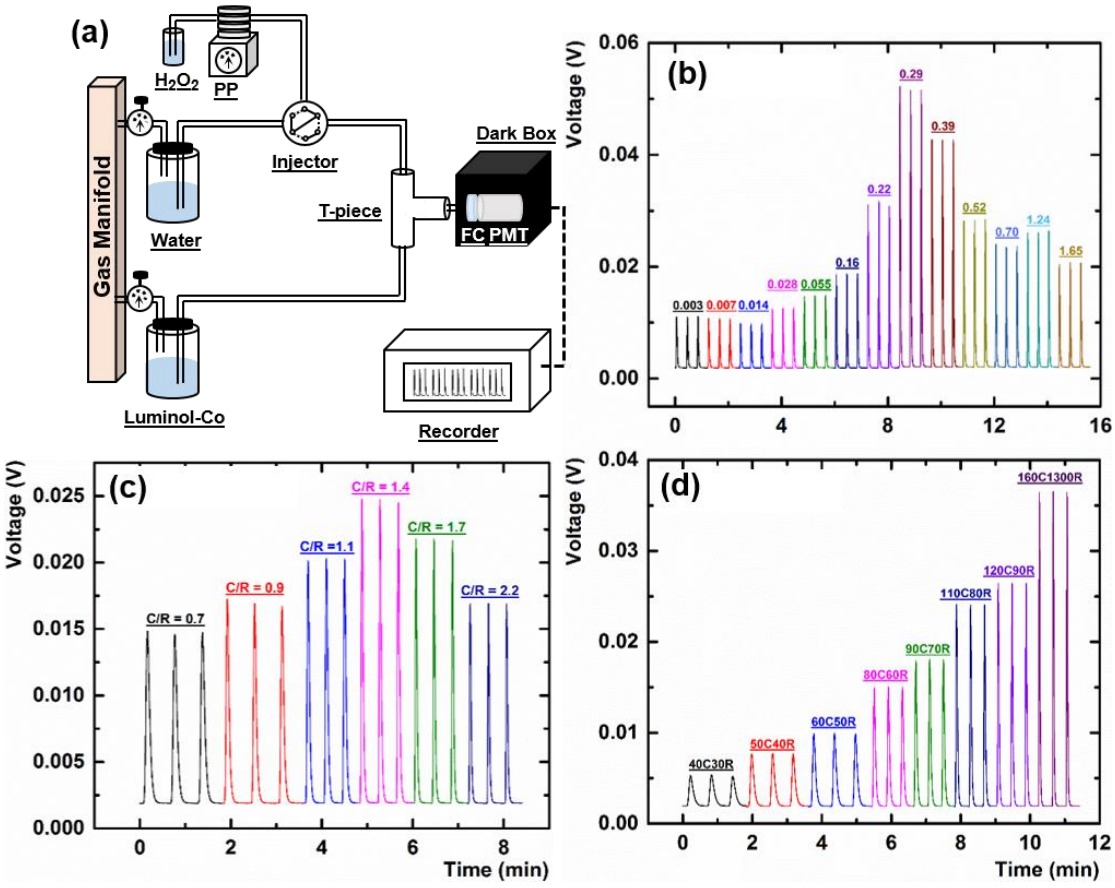

Figure 4. Chemiluminescence FIA system: (a) schematic of the experimental FIA CLD setup (PP – peristaltic pump, FC – flow-cell), (b) observed chemiluminescence peaks at different luminol concentrations as indicated in mM for three successive injections, (c) observed chemiluminescence peaks at different carrier/reagent pneumatic pressure ratios as indicated for three successive injections, (d) observed chemiluminescence peaks at different carrier and reagent pneumatic pressures in kPa as indicated by the numeral preceding C and R for the carrier and the reagent streams, respectively for three successive injections.

4.5 Chemiluminescence performance

The 3D printed radial flow-cell was compared with both the conventional coiled-tubing spiral flow-cell and the 3D printed spiral flow-cell with regard to analytical performance. All three flow-cells were compared using six different H_2O_2 standard concentrations, namely 100 nM, 200 nM, 400 nM, 800 nM, 1.6 μM, and 3.2 μM, the results from which are included in Figure 5 and Tables 1 and 2, and discussed below.

CLD using the 3D printed radial flow-cell provided an increase in the peak height (as shown in Figure 5 (a)) and peak area (as shown in the Supporting information (Figure S-2)) for all six H_2O_2 concentrations, as compared to both the coiled-tubing spiral flow-cell and the 3D printed spiral flow-cell. Compared to the coiled-tubing spiral flow-cell, the 3D printed radial flow-cell resulted in an average increase in the peak height of 63.5% and an average increase in the peak area of 89.4% as shown in Table 1. Compared to the 3D printed spiral flow-cell, the 3D printed radial flow-cell resulted in an average increase in the peak height of 58.5% and an average increase in the peak area of 89.5% as shown in Table 1. No significant differences in the peak

height or the peak area were observed between the coiled-tubing spiral flow-cell and the 3D printed spiral flow-cell. Excellent reproducibility was observed for all three flow-cells based upon three successive injections as shown in Table 1. A maximum RSD of 3.4%, 5.6%, and 3.0% was observed for the 3D printed radial flow-cell, the coiled-tubing spiral flow-cell, and the 3D printed spiral flow-cell, respectively, for the peak representing 100 nM H_2O_2, again as shown in Table 1.

Along with the peak height and peak area, the 3D printed radial flow-cell also resulted in an increase in the peak width for all six H_2O_2 concentrations as compared to both the other flow-cells, as shown in Figure 5 (b). The 3D printed radial flow-cell resulted in an average increase in the peak width of 41.3% and 42.0% as compared to the coiled-tubing spiral flow-cell, and the 3D printed spiral flow-cell, respectively as shown in Table 1. Again, no significant differences in the peak width were observed between the coiled-tubing spiral flow-cell and the 3D printed spiral flow-cell. An increase in the peak width was the result of an increase in the peak return and not the onset time, hence indicating an increase in the signal duration with the use of the 3D printed radial flow-cell as shown in Figure 5 (c). An onset time of 0.07 min (0.03 min from the injection to the start of the peak and 0.04 min from the start of the peak to the peak maxima) was observed for all three flow-cells at all six H_2O_2 concentrations. Representative chemiluminescence peaks for all three flow-cells at three different H_2O_2 concentrations, namely 100 nM, 800 nM, and 3.2 μM are shown in Figure 5 (d) for visual comparison.

All three flow-cells resulted in linear calibration plots for the peak height v/s concentration in two distinct regions, namely 100 nM to 400 nM and 800 nM to 3.2

μM, each with an $R^2 > 0.99$. As shown in Table 2, the 3D printed radial flow-cell resulted in a higher sensitivity as compared to both the other flow-cells in both the above-mentioned regions.

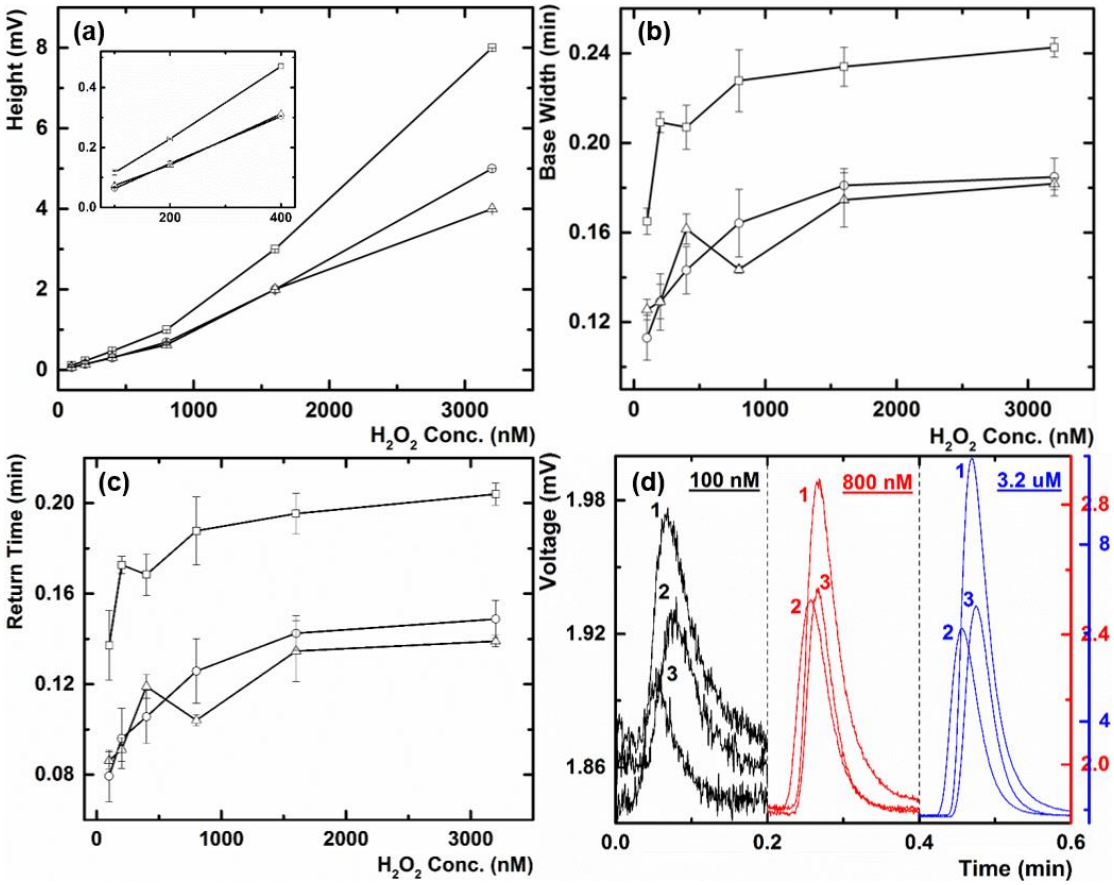

Figure 5. Chemiluminescence peak characteristics for the 3D printed radial flow-cell (□), the coiled-tubing spiral flow-cell (Δ), and the 3D printed spiral flow-cell (○): (a) peak heights at different H_2O_2 concentrations, the inset shows the magnified view of the peak height v/s concentration plot for the 100, 200, and 400 nM H_2O_2 concentrations. (b) peak base widths at different H_2O_2 concentrations, (c) peak return times at different H_2O_2 concentrations, and (d) representative chemiluminescence peaks at 100 nM, 800 nM, and 3.2 μM as indicated for the 3D printed radial flow-cell (1), the coiled-tubing spiral flow-cell (2), and the 3D printed spiral flow-cell (3).

458 Note: the chemiluminescence peaks in the sub figure (d) are not perfectly aligned on
459 the time axis due to their slightly different injection times.
460
461 Table 1. Comparison of the peak characteristics obtained with the 3D printed radial
462 flow-cell (3DP RFC), the coiled-tubing spiral flow-cell (SFC), and the 3D printed
463 spiral flow-cell (3DP SFC) at six different H_2O_2 concentrations.
464

H_2O_2 (nM)	Rel. % increase (peak height) using Radial Cell		Rel. % increase (peak area) using Radial Cell		Rel. % increase (peak width) using Radial Cell		% RSD (peak height)		
	Spiral (tube)	Spiral (3D)	Spiral (tube)	Spiral (3D)	Spiral (tube)	Spiral (3D)	3DP Radial	Spiral (tube)	Spiral (3D)
100	58.1	84.7	20.7	56.6	31.4	46.0	3.4	5.6	3.0
200	61.2	55.9	89.1	66.1	62.0	62.2	1.1	1.9	2.4
400	51.0	54.8	77.2	106.1	28.1	44.6	0.79	2.5	0.7
800	60.5	45.3	62.3	140.3	58.7	38.7	<0.01	2.1	2.0
1600	50.0	50.0	80.7	27.1	34.0	29.3	<0.01	<0.01	<0.01
3200	100.0	60.0	206.3	140.7	33.4	31.3	<0.01	<0.01	<0.01

465
466
467 Table 2. Calibration results for the 3D printed radial flow-cell (3DP RFC), coiled-
468 tubing spiral flow-cell (SFC), and the 3D printed spiral flow-cell (3DP SFC).

Parameter	100-400 nM H_2O_2			800-3200 nM H_2O_2		
	3DP RFC	SFC	3DP SFC	3DP RFC	SFC	3DP SFC
Linear Slope	1.2×10^{-6}	7.8×10^{-7}	8.0×10^{-7}	3.0×10^{-6}	1.3×10^{-6}	1.9×10^{-6}
Y-Intercept	-6.9×10^{-6}	-1.0×10^{-5}	-1.7×10^{-5}	-1.5×10^{-3}	-7.9×10^{-14}	-1.0×10^{-3}
R^2	0.9996	0.9925	0.9999	0.9972	0.9999	0.9999

469

4.6 Computational fluid dynamic simulated flow behaviour

Flow behaviour within the radial and spiral flow-cell designs were simulated and studied using computational fluid dynamic (CFD) calculations. Figures 6 (a) and 6 (b) demonstrates 100 simulated velocity streamlines in the radial flow-cell design and the spiral flow-cell design, respectively. As shown in Figure 6 (a), unidirectional velocity streamlines were observed in the radial flow-cell, originating from the inlet and terminating in the outlet. This indicates that the designed galley diameter of 1800 µm was found sufficient to prevent any recirculation from the galley into the channels. This was further validated through visual inspection by pumping food dye and by the absence of any split or odd chemiluminescence peaks resulting from the use of the 3D printed radial flow-cell.

The simulated fluid flow at the experimental flow rate of 800 $\mu L min^{-1}$ in both the radial flow-cell and spiral flow-cell designs was studied to understand the underlying mechanism for the increased response and improved sensitivity of the 3D printed radial flow-cell as compared to the coiled-tubing spiral flow-cell and the 3D printed spiral flow-cell. The respective positions of 100 representative flow streams at 0.25 simulated seconds in the radial flow-cell and spiral flow-cell designs are marked by the velocity colour coded balls in Figure 6 (a) and 6 (b), respectively. This indicates dispersion of flow streams over a higher area in the radial flow-cell design as compared to the spiral flow-cell design. Higher dispersion of the flow streams in the radial flow-cell design will enable higher spatial coverage by the generated chemiluminescence products in front of the PMT window. Higher spatial coverage in the radial flow-cell design especially near the inlet should contribute towards a more efficient transfer of the photons from the chemiluminescence reaction to the

photodetector, as the chemiluminescence intensity decays with time as per a first order rate equation [35]. Accordingly, this should contribute towards the observed relative increase in the peak area, peak height, and chemiluminescence sensitivity with the 3D printed radial flow-cell. Figures 6 (c) and 6 (d) demonstrate the velocity distributions in the radial flow-cell design and the spiral flow-cell design, respectively. This indicates that the radial flow-cell design results in ca. 10 times smaller linear velocities in the radial flow channels as compared to the spiral flow channel. Smaller linear velocities in the radial flow channels contribute towards the observed increase in the signal duration and a corresponding increase in the peak width [36].

A non-uniform flow velocity distribution was observed within the radial flow channels. Higher linear velocities were observed in the channels exiting near the outlet as compared to the channels exiting away from the outlet as shown in Figure 6 (c). This is due to a differential pressure drop experienced across the galley as shown in the Supporting Information (Figure S-3). This non-uniform flow velocity distribution among the radial flow channels did not result in any observed problems such as irreproducibility or peak distortion. However, the differential pressure drop across the galley and consequentially the non-uniform flow velocity distributions among the radial flow channels can be minimised in future by further optimisation of the galley dimensions and the outlet position. The individual velocity profiles in each radial flow channel and in each spiral turn are shown in the Supporting Information (Figures S-4 and S-5, respectively).

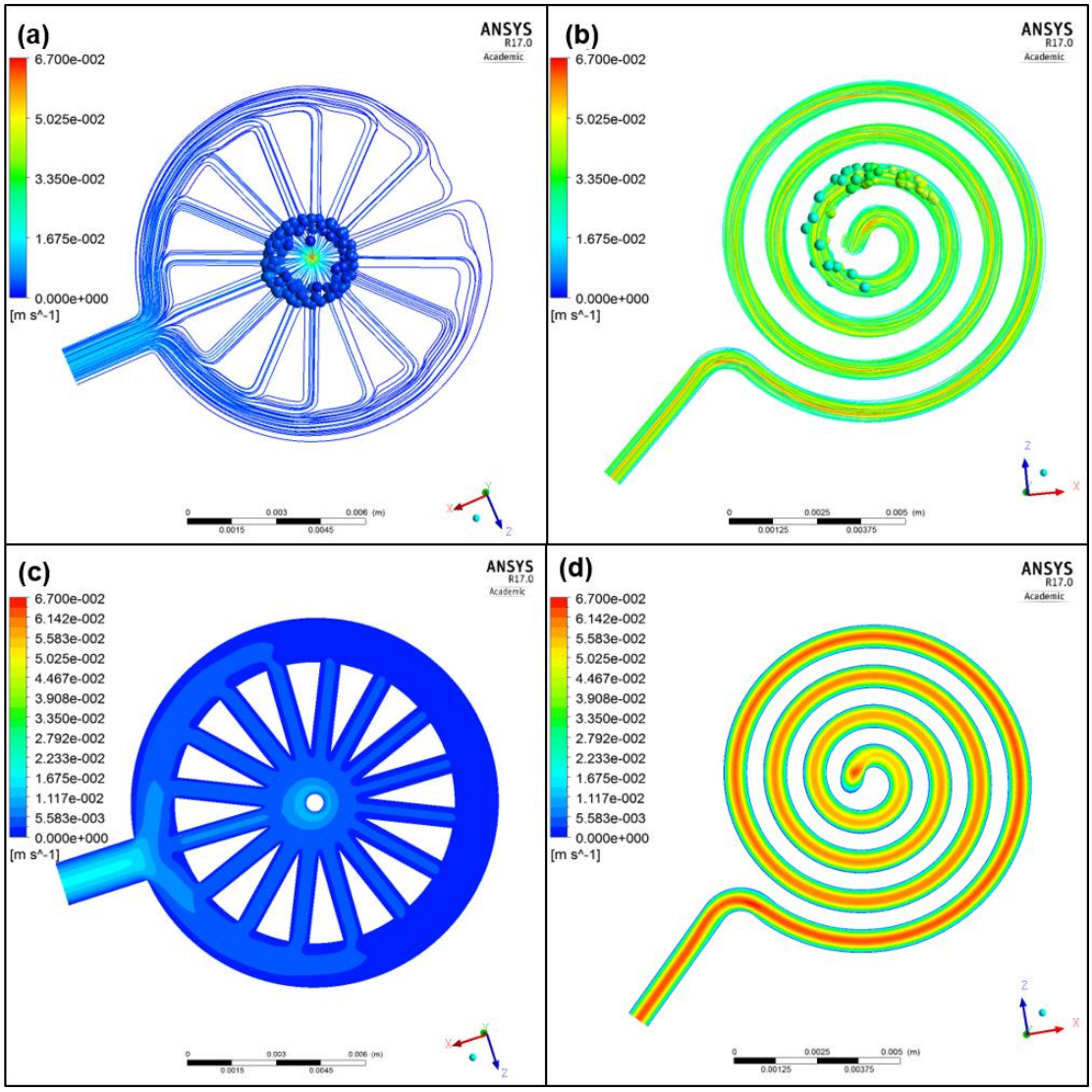

Figure 6. Computational fluid dynamic (CFD) simulated velocity streams and velocity contour plots at an inlet flow rate of 800 µL min^{-1}: (a) velocity streamlines in the radial flow-cell design and the representative flow at simulated 0.25 s is marked by velocity colour coded balls, (b) velocity streamlines in the spiral flow-cell design and the representative flow at simulated 0.25 s is marked by velocity colour coded balls, (c) velocity contour plot at mid plane of the radial flow-cell design, and (d) velocity contour plot at mid plane of the spiral flow-cell design.

4.7 Hydrogen peroxide in urine and coffee extracts

An IC-CLD system was developed to provide a fast and automated determination of urinary and coffee extract H_2O_2. It was assembled by substituting the sample carrier line from the T-piece (as shown in Figure 4 (a)) with the outlet from the cation exchange column. The IC method was developed using a cation exchange column packed with a sulphonated cation-exchanger and a water only mobile phase for the separation of H_2O_2 from otherwise interfering sample matrix ions [37]. Three IonPac® cation exchange columns were studied, namely CG10, CG11, and CS11, each with different particle and column sizes as mentioned above, assessing their chromatographic selectivity towards H_2O_2. In terms of overall chromatographic retention and efficiency, the CG10 proved most acceptable and was accordingly used for H_2O_2 separation. The CLD was performed with the above-mentioned luminol-Co(II) reagent using the new 3D printed radial flow-cell.

Urinary H_2O_2 was first observed by Varma and Devamanoharan [38] in 1990, since then it has been studied by several researchers [39-41]. H_2O_2 has been believed to produce damaging reactive oxygen species in the human body, although it also acts as a signalling molecule to regulate cellular processes [39]. The amount of H_2O_2 excreted in urine is linked to several activities [39], such as coffee drinking [42, 43], alcohol consumption [44], and exercise [45], and also several diseases [39], such as cancer [46], diabetes mellitus [47], respiratory distress syndrome [48], intestinal parasitic infection [49], Down's syndrome [50], and total body oxidative stress [28]. An increase in urinary H_2O_2 post-coffee drinking is partially linked to direct diffusion of H_2O_2 from coffee into the oral cavity and the upper gastrointestinal tract [51].

552 Traditionally, urinary H_2O_2 is measured using either an oxygen selective electrode
553 [52, 53] or the ferrous oxidation-xylenol orange (FOX) assay (and derivatives thereof)
554 [28, 47, 50]. However, oxygen selective electrodes have been found less sensitive for
555 urinary H_2O_2 [54] and suffer from frequent fouling. Additionally, the FOX assay
556 requires a long reaction time of ca. 60 min [28] and manual operation. Accordingly,
557 herein to demonstrate the practical application of the new flow cell and
558 simultaneously provide a potentially beneficial new IC-CLD method for urinary H_2O_2
559 determinations, an IC-CLD system was developed including the new 3D printed
560 radial flow-cell, and applied to H_2O_2 in urine and coffee extracts.
561
562 The developed IC-CLD system resulted in linear calibration plots from 1.25 µM to 5
563 µM H_2O_2 (slope = 3.86×10^{-4}, $R^2 = 0.9953$) and from 20 µM to 100 µM H_2O_2 (slope
564 = 1.78×10^{-3}, $R^2 = 0.9938$). Representative chemiluminescence chromatograms
565 obtained with eight H_2O_2 standards, namely 1.25 µM, 2.5 µM, 5 µM, 20 µM, 40 µM,
566 60 µM, 80 µM, and 100 µM are shown in Figure 7. Peak height %RSDs for the above
567 standards, based upon triplicate injections of each, were 9.19, 3.91, 5.80, 4.68, 2.63,
568 4.38, 1.90, and 1.14, respectively.
569
570 H_2O_2 peaks in the real samples were identified using the retention time of the H_2O_2
571 standards, and by spiking the real samples with known concentrations of H_2O_2. To
572 determine accuracy of the developed IC-CLD system, an unknown sample solution of
573 H_2O_2 was analysed first using a conventional FOX assay, and secondly with the
574 developed IC-CLD system. The FOX assay indicated the concentration of the
575 unknown H_2O_2 sample as 57.8 ± 1.2 µM, using a linear calibration ($R^2 = 0.9846$) plot
576 from 20 µM to 80 µM H_2O_2 (n= 3). Using the IC-CLD system, the concentration of

the unknown H_2O_2 sample was found as 57.6 ± 2.1 µM, here using a linear calibration (R^2 = 0.9974) plot from 20 µM to 80 µM H_2O_2 (*n*= 3). Calibration curves for the comparison assays can be found in the supporting information (Figure S-6).

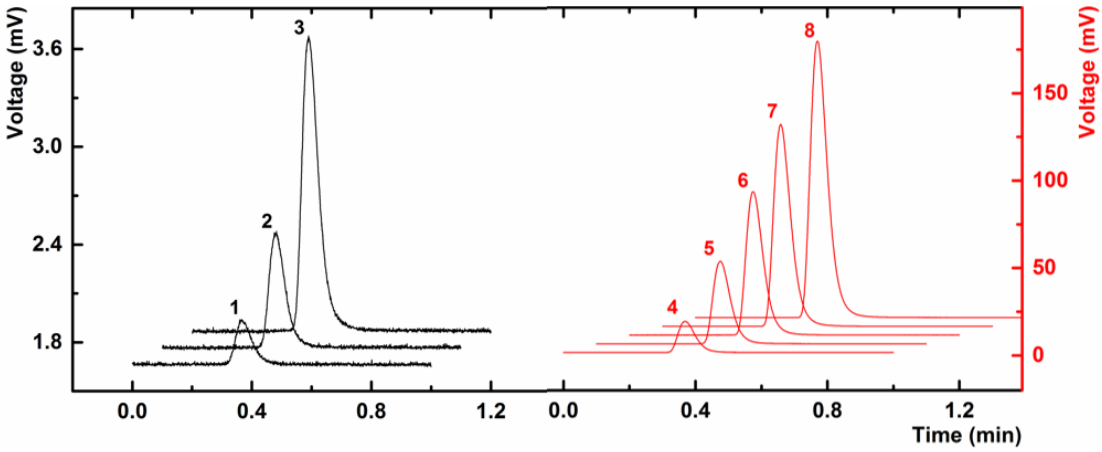

Figure 7. Representative chemiluminescence chromatograms for H_2O_2 standards with the developed IC-CLD system: 1.25 µM (1), 2.5 µM (2), 5 µM (3), 20 µM (4), 40 µM (5), 60 µM (6), 80 µM (7), and 100 µM (8).

Analysis of untreated urine samples using FIA resulted in a signal to noise ratio of less than 3, as shown in Figure 8 (a). This low signal to noise ratio was observed presumably due to significant matrix effects. Uric acid was identified as a significant interferent through interference studies. When urine samples were then directly passed through the CG10 column, to separate the H_2O_2 from the bulk of the unretained matrix, a split peak of H_2O_2 was observed, which was closely followed by unidentified negative and positive peaks, rendering the quantitative determination of urinary H_2O_2 impossible, as shown in Figure 8 (b). Following this, urine samples were first centrifuged at 2500 rcf for 8 min, in an attempt to remove any cellular debris and heavy proteins prior to the chromatographic separation. The IC-CLD chromatogram of the supernatant from the centrifuged urine samples provided a

smaller number of chemiluminescence peaks, as shown in Figure 8 (c), although a pronounced shoulder in the H_2O_2 peak and a baseline shift were still observed (Figure 8 (c)). Finally, to fully precipitate all urinary proteins, 2% w/v 5-sulfosalicylic acid was added to the supernatants of the centrifuged urine samples, and the solution was filtered through a 0.45 µm PTFE syringe filter. IC-CLD analysis of the resultant sample solutions recorded a single H_2O_2 peak and a stable baseline, as shown in Figure 8 (d). Urinary H_2O_2 was then determined in three separately processed urine samples (although all aliquoted from the same original sample). The urinary H_2O_2 in these samples was determined to be 2.5 ± 0.2 µM, using a linear calibration plot from 1.25 µM to 5 µM (R^2 = 0.9953). The measured urinary H_2O_2 concentration was found to be in agreement with that previously reported as being typical urinary H_2O_2 concentrations, namely 2.7 ± 1.2 µM (n = 29) in fresh urine samples, as measured by a modified FOX assay [28]. As seen in the UV chromatogram in Figure 8 (d), retention and co-elution of the remaining urinary components was evident, although completely separated from the chemiluminescence peak of H_2O_2.

The IC-CLD setup was then applied to the determination of the H_2O_2 concentration in coffee extracts. This assay did not require any prior sample preparation steps and the direct IC separation of freshly brewed coffee extracts resulted in a single H_2O_2 CLD peak, as shown in Figure 9. Once again the UV chromatogram shown in Figure 9 indicates the presence of other co-eluting coffee components. The H_2O_2 concentration in three coffee extract samples was determined as being 19.6 $\pm$ 0.3 µM, using a linear calibration plot from 20 µM to 80 µM (R^2 = 0.9974).

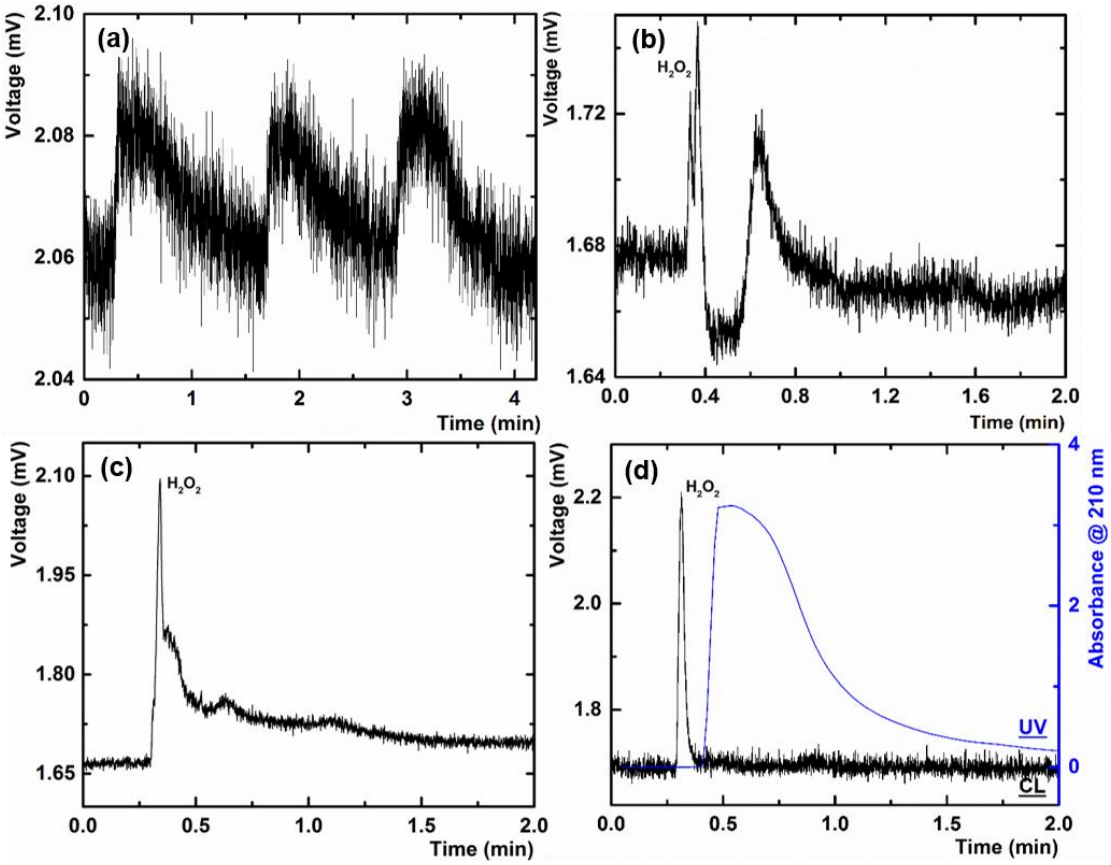

Figure 8. Effects of different sample treatment steps in the analysis of urinary H_2O_2: (a) chemiluminescence peaks obtained after direct injection of a fresh urine sample in the FIA CLD system for three successive injections, (b) chemiluminescence chromatogram obtained after direct injection of a fresh urine sample in the IC-CLD system, (c) chemiluminescence chromatogram obtained after injection of the supernatant from a centrifuged urine sample, and (d) chemiluminescence and UV recorded chromatograms obtained after injection of a 5-sulfosalicylic acid protein precipitated supernatant of a centrifuged urine sample.

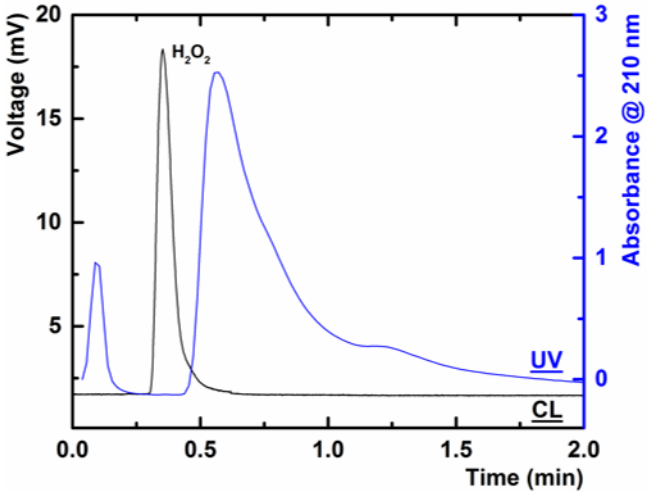

Figure 9. Chemiluminescence and UV recorded chromatograms obtained after injection of a fresh coffee extract sample in the IC-CLD system.

5 CONCLUSIONS

A new radial flow-cell design has been developed to (1) offer a less tortuous alternative to the conventional chemiluminescence flow-cell designs and (2) provide a higher chemiluminescence signal in terms of both the magnitude and the duration, as compared to the most commonly used spiral flow-cell design. Use of the radial flow-cell design enabled successful fabrication by 3D printing with closed channels for the first time. Owing to the less tortuous nature of the radial flow-cell, it only required 10 hours of post-PolyJet print processing time as compared to ca. 360 hours required for the tortuous spiral flow-cell and also facilitated a successful FDM print process. The radial flow-cell design also provided higher spatial coverage near the onset of the chemiluminescence reaction as compared to the spiral flow-cell design. Consequentially, the radial flow-cell design resulted in ca. 60% increase in the peak height and ca. 90% increase in the peak area as compared to the most commonly used spiral flow-cell design and hence enabling higher sensitivity CLD. Smaller linear velocities were observed in the radial flow channels as compared to the spiral flow

channel due to the parallel arrangement of the channels in the former. This resulted in ca. 40% increase in the signal duration with the radial flow-cell design as compared to the spiral flow-cell design and hence facilitating digital imaging analysis.

The 3D printed radial flow-cell was successfully applied within a novel IC-CLD assay for the determination of urinary and coffee extract H_2O_2.

6 ASSOCIATED CONTENT

6.1 Supporting Information

Supplementary data associated with this article can be found, in the online version, at

7 ACKNOWLEDGMENT

Funding from the Australian Research Council Centre of Excellence Scheme (Project Number CE 140100012) is gratefully acknowledged. This work was also supported by the Grant National Security Science and Technology Unit (NSSTU) on Counter Terrorism of the Department of Prime Minister and Cabinet of Australia.

8 REFERENCES

[1] C.A. Marquette, L.J. Blum, Applications of the luminol chemiluminescent reaction in analytical chemistry, Anal. Bioanal. Chem., 385 (2006) 546-554.

[2] A.J. Brown, P.S. Francis, J.L. Adcock, K.F. Lim, N.W. Barnett, Manganese (III) and manganese (IV) as chemiluminescence reagents: A review, Anal. Chim. Acta, 624 (2008) 175-183.

[3] J.L. Adcock, N.W. Barnett, C.J. Barrow, P.S. Francis, Advances in the use of acidic potassium permanganate as a chemiluminescence reagent: a review, Anal. Chim. Acta, 807 (2014) 9-28.

[4] P. Campıns-Falcó, L. Tortajada-Genaro, F. Bosch-Reig, A new flow cell design for chemiluminiscence analysis, Talanta, 55 (2001) 403-413.

[5] J. Burguera, A. Townshend, S. Greenfield, Flow injection analysis for monitoring chemiluminescent reactions, Anal. Chim. Acta, 114 (1980) 209-214.

[6] G. Rule, W.R. Seitz, Flow-injection analysis with chemiluminescence detection, Clin. Chem., 25 (1979) 1635-1638.

[7] H. Nakamura, Y. Murakami, K. Yokoyama, E. Tamiya, I. Karube, M. Suda, S. Uchiyama, A compactly integrated flow cell with a chemiluminescent FIA system for determining lactate concentration in serum, Anal. Chem., 73 (2001) 373-378.

[8] É. Tyrrell, C. Gibson, B.D. MacCraith, D. Gray, P. Byrne, N. Kent, C. Burke, B. Paull, Development of a micro-fluidic manifold for copper monitoring utilising chemiluminescence detection, Lab on a Chip, 4 (2004) 384-390.

[9] Y.-X. Guan, Z.-R. Xu, J. Dai, Z.-L. Fang, The use of a micropump based on capillary and evaporation effects in a microfluidic flow injection chemiluminescence system, Talanta, 68 (2006) 1384-1389.

[10] J.M. Terry, J.L. Adcock, D.C. Olson, D.K. Wolcott, C. Schwanger, L.A. Hill, N.W. Barnett, P.S. Francis, Chemiluminescence detector with a serpentine flow cell, Anal. Chem., 80 (2008) 9817-9821.

[11] A.M.G. Campaña, W.R. Baeyens, Chemiluminescence in Analytical Chemistry, Marcel Dekker Incorporated2001.

[12] S.D. Kolev, I.D. McKelvie, Advances in flow injection analysis and related techniques, Elsevier2008.

[13] N. Barnett, P. Francis, Chemiluminescence: overview, Encyclopedia of analytical science2005, pp. 506-511.

[14] J.L. Adcock, J.M. Terry, C.J. Barrow, N.W. Barnett, D.C. Olson, P.S. Francis, Chemiluminescence detectors for liquid chromatography, Drug Test Anal, 3 (2011) 139-144.

[15] J.M. Terry, E.M. Zammit, T. Slezak, N.W. Barnett, D.C. Olson, D.K. Wolcott, D.L. Edwards, P.S. Francis, Solution mixing and the emission of light in flow-cells for chemiluminescence detection, Analyst, 136 (2011) 913-919.

[16] C.I. Rogers, K. Qaderi, A.T. Woolley, G.P. Nordin, 3D printed microfluidic devices with integrated valves, Biomicrofluidics, 9 (2015) 016501.

[17] V. Gupta, M. Talebi, J. Deverell, S. Sandron, P.N. Nesterenko, B. Heery, F. Thompson, S. Beirne, G.G. Wallace, B. Paull, 3D printed titanium micro-bore columns containing polymer monoliths for reversed-phase liquid chromatography, Anal. Chim. Acta, 910 (2016) 84-94.

[18] S. Sandron, B. Heery, V. Gupta, D. Collins, E. Nesterenko, P.N. Nesterenko, M. Talebi, S. Beirne, F. Thompson, G.G. Wallace, 3D printed metal columns for capillary liquid chromatography, Analyst, 139 (2014) 6343-6347.

718 [19] S. Waheed, J.M. Cabot, N.P. Macdonald, T. Lewis, R.M. Guijt, B. Paull, M.C.
719 Breadmore, 3D printed microfluidic devices: enablers and barriers, Lab on a
720 Chip, 16 (2016) 1993-2013.
721 [20] K.B. Spilstead, J.J. Learey, E.H. Doeven, G.J. Barbante, S. Mohr, N.W. Barnett,
722 J.M. Terry, R.M. Hall, P.S. Francis, 3D-printed and CNC milled flow-cells for
723 chemiluminescence detection, Talanta, 126 (2014) 110-115.
724 [21] K.M. Scudder, C.H. Pollema, J. Ruzicka, The fountain cell: a tool for flow-
725 based spectroscopies, Anal. Chem., 64 (1992) 2657-2660.
726 [22] J.L. Perez Pavon, E. Rodriguez Gonzalo, G.D. Christian, J. Ruzicka, Universal
727 sandwich membrane cell and detector for optical flow injection analysis, Anal.
728 Chem., 64 (1992) 923-929.
729 [23] P.K. Dasgupta, Z. Genfa, J. Li, C.B. Boring, S. Jambunathan, R. Al-Horr,
730 Luminescence detection with a liquid core waveguide, Anal. Chem., 71 (1999)
731 1400-1407.
732 [24] P. Campíns-Falcó, L. Tortajada-Genaro, F. Bosch-Reig, A new flow cell design
733 for chemiluminiscence analysis, Talanta, 55 (2001) 403-413.
734 [25] N.r. Ibáñez-García, M. Puyol, C.M. Azevedo, C.S. Martínez-Cisneros, F.
735 Villuendas, M. Gongora-Rubio, A.C. Seabra, J.n. Alonso, Vortex configuration flow
736 cell based on low-temperature cofired ceramics as a compact
737 chemiluminescence microsystem, Anal. Chem., 80 (2008) 5320-5324.
738 [26] Y. Wen, H. Yuan, J. Mao, D. Xiao, M.M. Choi, Droplet detector for the
739 continuous flow luminol–hydrogen peroxide chemiluminescence system,
740 Analyst, 134 (2009) 354-360.
741 [27] D. Price, P.J. Worsfold, R. Fauzi, C. Mantoura, Determination of hydrogen
742 peroxide in sea water by flow-injection analysis with chemiluminescence
743 detection, Anal. Chim. Acta, 298 (1994) 121-128.
744 [28] J. Yuen, I. Benzie, Hydrogen peroxide in urine as a potential biomarker of
745 whole body oxidative stress, Free Radical Res., 37 (2003) 1209-1213.
746 [29] S.-X. Liang, L.-X. Zhao, B.-T. Zhang, J.-M. Lin, Experimental studies on the
747 chemiluminescence reaction mechanism of carbonate/bicarbonate and
748 hydrogen peroxide in the presence of cobalt (II), J. Phys. Chem. A, 112 (2008)
749 618-623.
750 [30] B.C. Gross, K.B. Anderson, J.E. Meisel, M.I. McNitt, D.M. Spence, Polymer
751 coatings in 3D-printed fluidic device channels for improved cellular adherence
752 prior to electrical lysis, Anal. Chem., 87 (2015) 6335-6341.
753 [31] K.B. Anderson, S.Y. Lockwood, R.S. Martin, D.M. Spence, A 3D printed fluidic
754 device that enables integrated features, Anal. Chem., 85 (2013) 5622-5626.
755 [32] P. Mahbub, P. Zakaria, R. Guijt, M. Macka, G. Dicinoski, M. Breadmore, P.N.
756 Nesterenko, Flow injection analysis of organic peroxide explosives using acid
757 degradation and chemiluminescent detection of released hydrogen peroxide,
758 Talanta, 143 (2015) 191-197.
759 [33] G.M. Greenway, T. Leelasattarathkul, S. Liawruangrath, R.A. Wheatley, N.
760 Youngvises, Ultrasound-enhanced flow injection chemiluminescence for
761 determination of hydrogen peroxide, Analyst, 131 (2006) 501-508.
762 [34] L. Marle, G.M. Greenway, Determination of hydrogen peroxide in rainwater
763 in a miniaturised analytical system, Anal. Chim. Acta, 548 (2005) 20-25.
764 [35] G. De Jong, N. Lammers, F. Spruit, U.A.T. Brinkman, R. Frei, Optimization of a
765 peroxyoxalate chemiluminescence detection system for the liquid

766 chromatographic determination of fluorescent compounds, Chromatographia, 18
767 (1984) 129-133.
768 [36] J.M. Terry, S. Mohr, P.R. Fielden, N.J. Goddard, N.W. Barnett, D.C. Olson, D.K.
769 Wolcott, P.S. Francis, Chemiluminescence detection flow cells for flow injection
770 analysis and high-performance liquid chromatography, Anal. Bioanal. Chem., 403
771 (2012) 2353-2360.
772 [37] T. Miyazawa, S. Lertsiri, K. Fujimoto, M. Oka, Luminol chemiluminescent
773 determination of hydrogen peroxide at picomole levels using high-performance
774 liquid chromatography with a cation-exchange resin gel column, J. Chromatogr.
775 A, 667 (1994) 99-104.
776 [38] S.D. Varma, P. Devamanoharan, Excretion of hydrogen peroxide in human
777 urine, Free Radic. Res. Commun., 8 (1990) 73-78.
778 [39] D.-H. Wang, K. Ogino, Y. Sato, N. Sakano, M. Kubo, K. Takemoto, C. Masatomi,
779 Urinary Hydrogen Peroxide as Biomarker, General Methods in Biomarker
780 Research and their Applications2015, pp. 313-331.
781 [40] N. Kuge, M. Kohzuki, T. Sato, Relation between natriuresis and urinary
782 excretion of hydrogen peroxide, Free Radical Res., 30 (1999) 119-123.
783 [41] S. Chatterjee, A. Chen, Functionalization of carbon buckypaper for the
784 sensitive determination of hydrogen peroxide in human urine, Biosens.
785 Bioelectron., 35 (2012) 302-307.
786 [42] L.H. Long, B. Halliwell, Coffee drinking increases levels of urinary hydrogen
787 peroxide detected in healthy human volunteers, Free Radical Res., 32 (2000)
788 463-467.
789 [43] K. Hiramoto, T. Kida, K. Kikugawa, Increased urinary hydrogen peroxide
790 levels caused by coffee drinking, Biol. Pharm. Bull., 25 (2002) 1467-1471.
791 [44] Y. Sato, K. Ogino, N. Sakano, D. Wang, J. Yoshida, Y. Akazawa, S. Kanbara, K.
792 Inoue, M. Kubo, H. Takahashi, Evaluation of urinary hydrogen peroxide as an
793 oxidative stress biomarker in a healthy Japanese population, Free Radical Res.,
794 47 (2013) 181-191.
795 [45] E. Deskur, P. Dylewicz, Ł. Szczęśniak, T. Rychlewski, M. Wilk, H. Wysocki,
796 Exercise-induced increase in hydrogen peroxide plasma levels is diminished by
797 endurance training after myocardial infarction, Int. J. Cardiol., 67 (1998) 219-
798 224.
799 [46] D. Banerjee, U. Madhusoodanan, S. Nayak, J. Jacob, Urinary hydrogen
800 peroxide: a probable marker of oxidative stress in malignancy, Clin. Chim. Acta,
801 334 (2003) 205-209.
802 [47] D. Banerjee, J. Jacob, G. Kunjamma, U. Madhusoodanan, S. Ghosh,
803 Measurement of urinary hydrogen peroxide by FOX-1 method in conjunction
804 with catalase in diabetes mellitus−a sensitive and specific approach, Clin. Chim.
805 Acta, 350 (2004) 233-236.
806 [48] M. Mathru, M.W. Rooney, D.J. Dries, L.J. Hirsch, L. Barnes, M.J. Tobin, Urine
807 hydrogen peroxide during adult respiratory distress syndrome in patients with
808 and without sepsis, Chest, 105 (1994) 232-236.
809 [49] S. Chandramathi, K. Suresh, Z. Anita, U. Kuppusamy, Elevated levels of
810 urinary hydrogen peroxide, advanced oxidative protein product (AOPP) and
811 malondialdehyde in humans infected with intestinal parasites, Parasitology, 136
812 (2009) 359-363.

[50] C. Campos, R. Guzmán, E. López-Fernández, Á. Casado, Evaluation of urinary biomarkers of oxidative/nitrosative stress in adolescents and adults with Down syndrome, Life Sci., 89 (2011) 655-661.
[51] B. Halliwell, K. Zhao, M. Whiteman, The gastrointestinal tract: a major site of antioxidant action?, Free Radical Res., 33 (2000) 819-830.
[52] L.H. Long, P.J. Evans, B. Halliwell, Hydrogen peroxide in human urine: implications for antioxidant defense and redox regulation, Biochem. Biophys. Res. Commun., 262 (1999) 605-609.
[53] B. Halliwell, M.V. Clement, L.H. Long, Hydrogen peroxide in the human body, FEBS Lett., 486 (2000) 10-13.
[54] B. Halliwell, J. Gutteridge, Oxidative stress, Free radicals in biology and medicine, Oxford University Press, New York, 2007, pp. 297-299.

827 **Graphical Abstract**

828

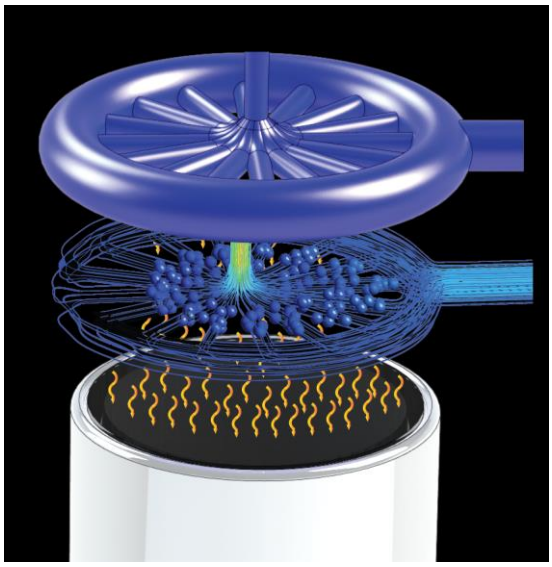

829